New Lagrangian diagnostics for characterizing fluid flow mixing

Ruty Mundel, Erick Fredj, Hezi Gildor, and Vered Rom-Kedar

Citation: Physics of Fluids (1994-present) **26**, 126602 (2014); doi: 10.1063/1.4903239
View online: http://dx.doi.org/10.1063/1.4903239
View Table of Contents: http://scitation.aip.org/content/aip/journal/pof2/26/12?ver=pdfcov
Published by the AIP Publishing

PHYSICS OF FLUIDS **26**, 126602 (2014)

New Lagrangian diagnostics for characterizing fluid flow mixing

Ruty Mundel,[1] Erick Fredj,[2] Hezi Gildor,[3] and Vered Rom-Kedar[4,a)]
[1]*The Hebrew University of Jerusalem, Jerusalem 91904, Israel*
[2]*Department of Computer Science, Jerusalem College of Technology, Jerusalem 91160, Israel*
[3]*Institute of Earth Sciences, The Hebrew University of Jerusalem, Jerusalem 91904, Israel*
[4]*The Estrin Family Chair of Computer Science and Applied Mathematics, Weizmann Institute of Science, Rehovot 76100, Israel*

(Received 11 February 2014; accepted 15 September 2014; published online 15 December 2014)

A new kind of Lagrangian diagnostic family is proposed and a specific form of it is suggested for characterizing mixing: the extreme (maximal/minimal) extent of a trajectory and some of its variants. It enables the detection of coherent structures and their dynamics in two- (and potentially three-) dimensional unsteady flows in both bounded and open domains. Its computation is simple and provides new insights regarding the mixing properties on both short and long time scales and on both spatial plots and distribution diagrams. We demonstrate its applicability to two dimensional flows using two toy models and a data set of surface currents from the South Atlantic. © *2014 AIP Publishing LLC.* [http://dx.doi.org/10.1063/1.4903239]

I. INTRODUCTION

Visualizing and quantifying mixing in unsteady fluid flows is a magical and tricky business, with important practical implications including larval dispersion and population connectivity,[1,2] oil spills,[3,4] search and rescue,[5,6] functioning of the marine ecological system,[7] and more.[8] Currently, there are many tools to visualize and analyze mixing properties of flows and maps.[9–17] While this field provides an endless source of scientifically produced art, beyond its aesthetic nature lurks the scientific challenge of characterizing these complex phenomena and providing predictions and insights relevant for real life problems.

One aspect of the complexity arises from the flow field structure. Unsteady flow fields typically have a mixture of Coherent Structures (CSs), jets, and mixing layers that move in an unsteady fashion. Moreover, these structures typically exist only for some finite time. Roughly, by coherent structure, we mean a body of fluid which moves together for a certain period of time in any reference frame one chooses, namely, we take the Lagrangian point of view which is frame independent (see discussion and references in Refs. 15, 18, and 19). Passive particles placed inside such a coherent structure remain in it as long as it lives, often moving roughly quasi-periodically around the coherent structure center. Here, we mainly focus on such CSs. Jets may be characterized as regular particles that flow between neighboring sections. These structures are typically separated by mixing layers, the regions in which there is "chaotic mixing"—a sensitive dependence of the Lagrangian trajectories on initial conditions (i.c.). Particles belonging to the mixing layer may stick to a nearby coherent structure or a jet for a certain period and then eject from it. This complex mixture of structures may appear in flows in closed domains (such as closed basins), in open domains (such as coastal areas), or in practically unbounded domains (such as eddies within the Pacific Ocean).

Another aspect of the complexity is the infinite dimensional nature of the initial data problem.[17,20,21] Indeed, the initial distribution of the particle density belongs to the space of all possible

a)Author to whom correspondence should be addressed. Electronic mail: vered.rom-kedar@weizmann.ac.il

initial distributions of scalar fields. Different mixing characteristics may apply to particular subclasses of such distributions.[22,23]

The last aspect we mention here is the temporal complexity of the problem. There are the classical mixing time scales associated with the molecular diffusion and viscosity, relevant for both steady and unsteady flows. However, for unsteady flows, additional scales emerge,[24,25] those associated with the unsteady component frequencies and amplitudes and those associated with the resulting chaotic mixing scales. Finally, in many applications, the observation time scale is also relevant.[18,26]

Defining a proper characterization of mixing is non-trivial and is problem and application-oriented. With all these complexities in mind, with the common appearance of mixture of flow regimes having temporal variations, we conclude that any classification scheme of mixing domains must have some tunable threshold parameters. On a finite time regime, most characteristics do not reach their asymptotic values, hence to distinguish between different types of trajectories (i.e., belonging to different structures or regions), threshold parameters need to be introduced. For example, to distinguish between a mixing layer and coherent motion on a finite time interval, a threshold parameter for Finite Time Lyapunov Exponent (FTLE), Finite Size Lyapunov Exponent (FSLE), or for Relative Dispersion (RD) is commonly used, either *a priori* or *a posteriori*. This observation impedes the quest for universal, parameter-free classification. Indeed, despite being a classical long standing problem, new mixing characteristics are suggested and presented in various ways, from both Eulerian and Lagrangian points of view.[10,15,16,27–30]

Eulerian characteristics correspond to snapshots (or temporal averages) of the velocity field or its spatial derivatives (e.g., the Okubo-Weiss criterion or the vorticity field[31,32]). Numerous studies in recent years developed methods to detect mesoscale eddies, relying on analysis of oceanic Eulerian measurements, such as velocities, Sea Surface Height (SSH), or Sea Surface Temperature (SST).[33–35]

Lagrangian characteristics are based on an integrative procedure by which an observable is measured along trajectories (e.g., the absolute dispersion (AD) measures the distance travelled by a particle, the RD measures the distance between a particle and its neighbors, the FTLE measures the maximal local stretching rate, etc.). Some of the Lagrangian characteristics present the resulting observable after a certain integration time, with no information on the intermediate time dynamics (e.g., the AD and RD fields depend only on the initial and final locations of the particles), whereas some of the other Lagrangian characteristics use averaging or integration along the trajectories.[3,17,26,36–38] These Lagrangian fields are commonly used to identify regions of small and enhanced stretching and, in particular, are used to identify the spatial position of dividing surfaces between different regions.[2,26,27] Another approach, mainly applicable for time-dependent open flow is based on the residence time that particles spend in a certain domain.[30,39] The locations and sizes of CSs have been mainly studied by the transfer-operator approach, providing a connection between the Eulerian and Lagrangian perspectives.[15,40–42] More recently, the notion of coherent Lagrangian vortices was introduced to identify CSs by using a variational principle on the averaged Lagrangian strain.[19] The notion of maximal absolute dispersion was first introduced for studying the lobe dynamics[43] of surface particles embedded in a three dimensional velocity field.[44] This study has motivated much of the current work.

Here, we propose a new family of Lagrangian characteristics: the spatial dependence of extreme values of an observable along trajectories. Since asymptotically these values converge to common extreme values in each ergodic component (similarly to Lagrangian averages along trajectories, in particular, this is the main feature of the ergodic partition approaches[3,17,36]), such extrema fields provide a rough division into distinguishable ergodic components. Moreover, the extreme values of the selected observable may by themselves have significant physical meaning. Examples of such significant observable values are: Maximal/Minimal Extension of Trajectories in a certain direction (hereafter MET), maximal speed or strain experienced by the particle, closest approach to the particle initial location, or closest approach to a prescribed location. In fact, any of the commonly calculated Lagrangian fields may be chosen as an observable.

Here, we focus on the MET and its variants, such as the average between the minimal and maximal extents and their difference (hereafter we refer to all of these as MET). These new MET characteristics have a few advantages. First, their computation is simple and intuitive and their computational cost is relatively low. Second, by definition their convergence in time is non-oscillatory. Third,

and most important, by choosing the MET and examining its Probability and Cumulative Distribution Functions (PDF and CDF), we can extract not only the existence of CSs, but can also quickly determine many of their characteristics (e.g., their number, size, and location). This feature will potentially allow for a substantial data reduction; see below.

Studying extreme value statistics (EVS) in the context of chaotic dynamical systems is a fascinating relatively new field of research.[45–50] Previous works on the extreme values of an observable of dynamical systems have mostly focused on the temporal dependence of a single chaotic trajectory for maps (mainly for chaotic dissipative maps), connecting it to the universal distributions appearing in the field of EVS on one hand and to Poincaré recurrences and local dimensionality of the attractors on the other hand (the connection to Refs. 36 and 48 may thus be intriguing). Here, we focus instead on utilizing the extreme value functionals as convenient spatial characteristics of dynamical systems with mixed phase space. A related approach in the study of the spatial structure of resonances in the standard map has been previously proposed, where differences between supremum and infimum along trajectories (minus the averaged rotations) was related to the width of a resonance.[45]

The paper is ordered as follows: we first define the new family of characteristics (Sec. II) and explore their properties using a few toy models (Sec. III). We then apply these measures to real geophysical data—surface currents in the South Atlantic (Sec. IV). We conclude and discuss some of the future directions in Sec. V.

II. MAIN CONCEPTS AND DEFINITIONS

Consider the motion of passive particles in a fluid flow (see specific examples below)

$$\frac{dx}{dt} = u(x,t), \qquad x \in \mathbb{R}^n,\ n = 2 \text{ or } 3 \tag{1}$$

and the extremal (and its variants) values of an observable function ϕ for each particle along a time segment of a trajectory

$$M_\phi^+(\tau; x_0, t_1) = \max_{t\in[t_1,t_1+\tau]}\phi(x(t;t_0)), \tag{2}$$

$$M_\phi^-(\tau; x_0, t_1) = \min_{t\in[t_1,t_1+\tau]}\phi(x(t;t_0)), \tag{3}$$

$$M_\phi^{shift}(\tau; x_0, t_1) = M_\phi^+(\tau; x_0, t_1) - M_\phi^-(\tau; x_0, t_1), \tag{4}$$

$$M_\phi^{mean}(\tau; x_0, t_1) = \frac{1}{2}(M_\phi^+(\tau; x_0, t_1) + M_\phi^-(\tau; x_0, t_1)), \tag{5}$$

where $x(t_0;t_0) = x_0$ and $t_1 \in \mathbb{R}$. Notice there are three time parameters in the above definition: t_0 corresponds to the seeding time of the particles—the velocity field phase at which the integration of the trajectories begins. $[t_1, t_1+\tau]$ is the extremal window, the recording time interval on which the observable is maximized/minimized. One natural choice is to take $t_1 = t_0$ and τ sufficiently large with respect to the CS turnover time, so that the CS is resolved within the extremal window. For periodic flows, shifting the extremal window may reveal trapping regions of the CSs. For unsteady flows, when coherent structures emerge and disappear or move around in an unknown manner, windowing in t_1 and τ may reveal the temporal existence and spatial movement of CSs, see below. Notice that $M_\phi^{shift}(0; x_0, t_0) = 0, M_\phi^{mean}(0; x_0, t_1) = M_\phi^+(0; x_0, t_1) = M_\phi^-(0; x_0, t_1) = \phi(x(t_1; t_0))$ and that $M_\phi^{shift}(\tau; x_0, t_1)$, $M_\phi^+(\tau; x_0, t_1), -M_\phi^-(\tau; x_0, t_1)$ are nondecreasing functions of $|\tau|$.

Asymptotically, we define

$$M_\phi^+(x_0) = \limsup_{t\to\infty}\phi(x(t;t_0)), \tag{6}$$

$$M_\phi^-(x_0) = \liminf_{t\to\infty}\phi(x(t;t_0)), \tag{7}$$

$$M_\phi^{shift}(x_0) = M_\phi^+(x_0) - M_\phi^-(x_0), \tag{8}$$

$$M_\phi^{mean}(x_0) = \frac{1}{2}(M_\phi^+(x_0) + M_\phi^-(x_0)), \tag{9}$$

with similar definitions for the negative time asymptotic.

These definitions naturally extend to maps. Indeed, for time-periodic flows, when the observation time includes many periods, it makes sense to consider the discrete time series found from the Poincaré map (the stroboscopic sampling of the signal) instead of the continuous flow, and all the above notions apply (e.g., notice that $M_{\phi}^{shift}(x_0)$ is very similar to the width function that was previously used in studying the standard map[45]). Here, however, for deductive reasons we do not use the time-periodicity feature of the toy models. Instead, we keep in mind the general setting for geophysical flows where the velocity field is not periodic and in principle even when there is a known dominant frequency in the spectrum (e.g., tidal frequency) the observation time may be shorter than the associated period.

We focus on the MET fields by setting the observable ϕ to measure the extent of the particle position in a given direction $\mathbf{r}$: $\phi(x(t;t_0)) = x(t;t_0)\cdot\mathbf{r}$. $M_{\mathbf{r}}^{\pm}(\tau;x_0,t_1)$ represent the maximal/minimal extents visited by the particle during the extremal window $[t_1,t_1+\tau]$. $M_{\mathbf{r}}^{shift}(\tau;x_0,t_1)$ denotes the difference between these maximal and minimal extents, and is called the **maximal shift**. $M_{\mathbf{r}}^{mean}(\tau;x_0,t_1)$ denotes the mean of the maximal and minimal extents, and is called hereafter the **Mean of Extrema EXtents—MEEX**.

We propose that by monitoring these fields, which are trivial to compute, we can infer quite a few properties of the Lagrangian flow structure both asymptotically and transiently. Moreover, we propose that such properties may be found quite efficiently by analyzing the PDF and CDF of the MET field. This may lead to significant data reduction from 2D fields (e.g., the common FTLE or RD) to a 1D plot. Often, especially in realistic geophysical applications, the amount of data (e.g., data extracted from satellites or from general circulation models) is huge and time-dependent, and efficient data-compression methods are needed. As described in Sec. III, the shape of the CDF provides information about the existence of coherent structures, their locations, and the existence of chaotic zones. It seems that some of the properties may even be inferred from a sampling of the flow field in only a few directions, making this diagnostic a potentially useful tool in real applications where practically there is a limited sampling of the flow (e.g., by only few drifters). Potentially this approach may be also applicable in the fully three dimensional setting. We will further explore this direction in future studies.

III. TYPICAL FEATURES OF THE MET: TOY MODELS

Next we examine the properties of the extremal fields at typical structures that appear in unsteady flows. To this aim, we first consider prototypical models for stirring and mixing in bounded domains—the steady and time-dependent double gyre models. We then consider the oscillating vortex pair (OVP) model to demonstrate the method on a flow in an unbounded domain.

A CS, loosely defined as a group of trajectories with a common averaged behavior on some fast eddy-turnover time scale, may be stationary, gently oscillating, rotating, or advected in an unbounded domain. The FTLE and RD fields for particles in all such structures asymptotically vanish. Below, we list the characteristic features of the MET in these different settings. We show that while the MET is simpler to compute, it provides additional information about the properties of the coherent structures.

A. Coherent structures in bounded domains

To gain intuition, we examine the double gyre model[27]

$$\begin{aligned}\Psi_{xy}(x,y,t) &= -A\sin(\pi f(x,t))\sin\pi y \\ f(x,t) &= \epsilon\sin\omega t\, x^2 + (1-2\epsilon\sin\omega t)x.\end{aligned} \tag{10}$$

We begin with the trivial case of the steady double gyre ($\epsilon = 0$) and then continue to more realistic settings. In this and all other cases (except Figs. 6 and 7 in which sensitivity to resolution is studied) we seed the double gyre domain $[0,2]\times[0,1]$ by uniformly spaced 400×200 initial values, integrating the equations of motion with Matlab ode45 solver.

A single stationary coherent structure. Consider the stationary double gyre model. The maximal and minimal extents in the x direction for this case are shown in Figs. 1(a) and 1(d). The flow has two symmetric gyres lying along the horizontal direction and no mixing zone. Examine the

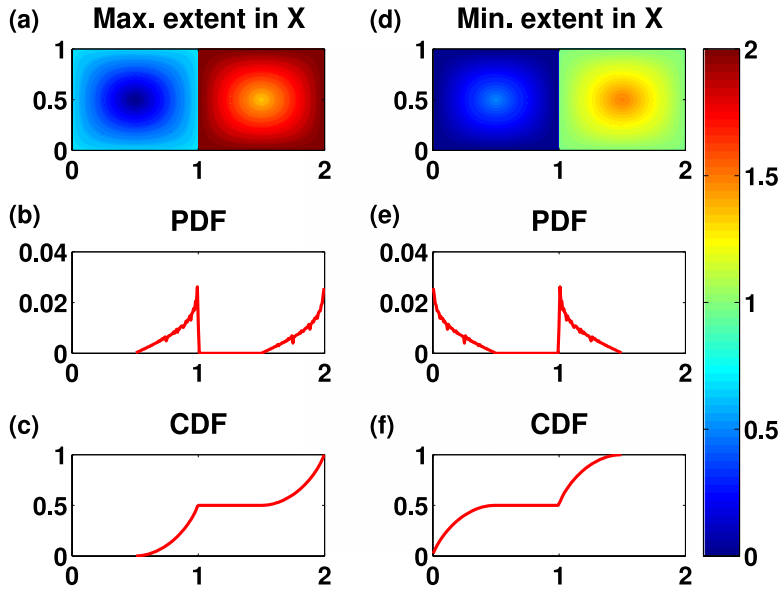

FIG. 1. Two stationary coherent structures: the maximal (left) and minimal (right) x position ($M^{\pm}_{(\mathbf{1},\mathbf{0})}$) of all initial conditions is plotted (top), as are the corresponding PDF (middle) and CDF (bottom) functions. Each gyre appears in the PDF and correspondingly in the CDF: the left gyre accumulates to occupy exactly half of the domain, as apparent from the height of the CDF plateau region. For the maximal extent CDF (left column), the CS center at $x = 0.5$ is identified by the CDF parabolic rise and its maximal extent, up to $x = 1$, is identified as the plateau left boundary. Corresponding identifiable signatures apply to the right gyre and to the minimal extent CDF (right column). Equation (10), $A = 0.25$, $\epsilon = 0$, and $\tau = 200$.

left gyre first. All trajectories belonging to the left gyre are bounded and periodic in time. Hence, for any fixed t_1, for all τ, $M_{\mathbf{r}}(\tau; x_0, t_1)$ and $M^{\pm}_{\mathbf{r}}(\cdot)$ are finite and, for sufficiently large τ, $M^{shift}_{\mathbf{r}}(\cdot)$ is equal to the width of the periodic orbit in the direction $\mathbf{r}$, whereas $M^{\pm}_{\mathbf{r}}$ provide the maximal and minimal extents in this direction.

Asymptotic form of the PDF and CDF. The PDFs and CDFs for this case are also shown in Fig. 1. The CDF of $M^{+}_{\mathbf{r}}$ converges to a piecewise smooth increasing function which starts increasing quadratically from zero concentration at the coherent structure center ($x = 0.5$) and abruptly stops increasing at the coherent structure boundary ($x = 1.0$). The area fraction of the left coherent structure is given by the CDF height difference between the two corresponding plateaus of the CDF. The CDF of $M^{-}_{\mathbf{r}}$ (Fig. 1(f)) starts increasing abruptly at the coherent structure leftmost boundary ($x = 0$) and stops increasing quadratically at the coherent structure center ($x = 0.5$) in a plateau. For the $M^{-}_{\mathbf{r}}$ CDF, the area fraction of the left coherent structure is given by the CDF height difference between the corresponding plateau of this CDF and the origin.

Several stationary coherent structures. The properties of the four quantifiers $M^{shift}_{\mathbf{r}}, M^{mean}_{\mathbf{r}}$, $M^{\pm}_{\mathbf{r}}$, and the directional dependence are clarified when several coherent structures coexist in the flow. Figs. 2(a)-2(h) show these four fields for two directions (x and y). First, we observe that the $M^{\pm}_{\mathbf{r}}$ fields distinguish between different CSs provided that the structures have no overlap in the direction $\mathbf{r}$. In our example, it is clear that the x maximal/minimal extent fields ($M^{\pm}_{(\mathbf{1},\mathbf{0})}$, Figs. 1, 2(e) and 2(f)) distinguish between the left and right gyres whereas the y maximal/minimal extent fields ($M^{\pm}_{(\mathbf{0},\mathbf{1})}$, Figs. 2(a) and 2(b)) do not. More generally, denote by L_{x-left} the x coordinate of the right boundary of the left gyre, by $(C_{x-right}, C_{y-right})$ the center of the right gyre, and by L_y the height of the gyres. Then, for $\mathbf{r} = (r_x, r_y)$, we see that $M^{+}_{\mathbf{r}}$(i.c. in left gyre) $= \max_{\text{i.c. in left gyre}}(x(t)r_x + y(t)r_y) < L_{x-left}r_x + L_y r_y$ whereas $M^{+}_{\mathbf{r}}$(i.c. right gyre) $= \max_{\text{i.c. in right gyre}}(x(t)r_x + yr_y) > C_{x-right}r_x + C_{y-right}r_y$. Hence, if there is a gap between the two bounds (here $\frac{r_y}{r_x} < \frac{C_{x-right} - L_{x-left}}{L_y - C_{y-right}}$), we will call $\mathbf{r}$ a **resolving direction** and then the CDFs of $M^{\pm}_{\mathbf{r}}$ show two distinct monotone increasing regimes, each corresponding to a different gyre as in Fig. 1. In contrast, the $M^{shift}_{\mathbf{r}}$ field is identical for the two gyres. More generally, for all $\mathbf{r}$, since the $M^{shift}_{\mathbf{r}}$ field measures the spatial extent in

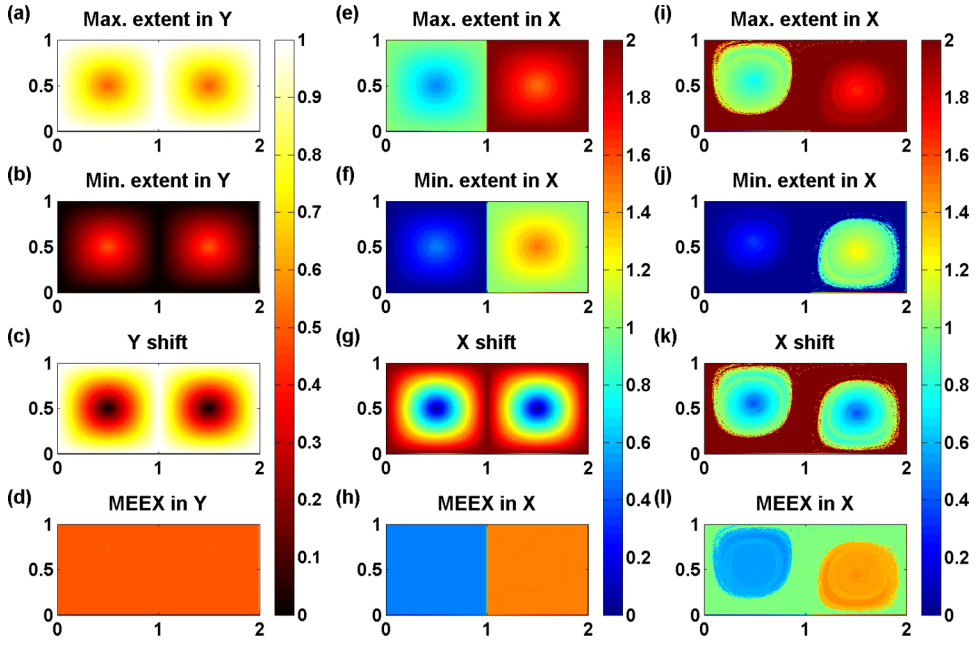

FIG. 2. Two stationary (a)-(h) and oscillatory (i)-(l) coherent structures. (a)-(d) The need to choose a resolving direction for obtaining the number of distinct CSs from the corresponding CDFs is demonstrated. The two gyres here have exactly the same extent in the y direction (i.e., identical $M^{\pm}_{(\mathbf{0},\mathbf{1})}$ values) hence the CDF of the $M^{\pm}_{(\mathbf{0},\mathbf{1})}$ does not lead to a distinction between the left and right gyres. (e)-(h) The need for the maximal/minimal quantifiers is demonstrated—while the maximal/minimal x values ($M^{\pm}_{(\mathbf{1},\mathbf{0})}$) (e) and (f) distinguish between the right and left gyres, their difference, the maximal shift $M^{shift}_{(\mathbf{1},\mathbf{0})}$ (g), does not. The MEEX in x, $M^{mean}_{(\mathbf{1},\mathbf{0})}$ (h), distinguishes between the gyres yet remains constant throughout the gyre, namely, it does not resolve the inner gyre structure. (i)-(l) The applicability to unsteady flow is demonstrated (Eq. (10) with $A = \epsilon = 0.25$, $\omega = 2\pi/10$, and $\tau = 200$). Notice that in both the stationary and oscillatory cases, at the coherent structure centers the fields $M^{shift}_{\mathbf{r}}$, $M^{+}_{\mathbf{r}}$, $-M^{-}_{\mathbf{r}}$ attain their local minima, whereas $M^{mean}_{\mathbf{r}}$ appears to be approximately constant along each gyre (as a result of the symmetric form of the gyres). In the stationary cases (a), (b), (e), and (f) the value of $M^{\pm}_{\mathbf{r}}$ at the center matches the center position whereas in the oscillatory case (i) and (j) there is a mismatch due to the oscillation: $M^{\pm}_{\mathbf{r}} - x_c(t_0;t_0)\cdot\mathbf{r} \neq 0$.

the direction $\mathbf{r}$ of the gyres, all coherent structures are generally lumped together in the CDF of the $M^{shift}_{\mathbf{r}}$ field (similarly to the CDF of the standard FTLE and RD fields). Finally, while the $M^{mean}_{\mathbf{r}}$ field distinguishes between the gyres, it is not necessarily monotone within the gyre and thus may produce a more complex CDF (see e.g., Fig. 3).

More generally, we see that depending on the structures' alignments, a direction $\mathbf{r}$ may or may not resolve the structures. If the center of one structure is bounded away from the maximal (or minimal) extent of the other in the direction $\mathbf{r}$ we do have separation—a gap in the $M^{\pm}_{\mathbf{r}}$ values. We expect to be able to find such resolving directions when there is a small number of coherent structures, but not when there are many possibly disordered structures in the domain (as in 2D-turbulent flows). In such cases, one can subdivide the domain until the structures are resolved; see Secs. IV and V.

The important conclusion from the above is that the CDF of the $M^{mean}_{\mathbf{r}}$ and $M^{\pm}_{\mathbf{r}}$ fields with a resolving direction $\mathbf{r}$ may be used to distinguish between the existence of multiple vs. a single CSs (thus helping in data reduction). In contrast, the CDF of the $M^{shift}_{\mathbf{r}}$ field, of the MET in nonresolving directions, of the RD, FTLE fields, and of other similar fields cannot help in counting the number of distinct CSs.

Oscillating coherent structures and the mixing layer. Consider now the periodically perturbed double gyre model shown in Figs. 2(i)-2(l). Here, trajectories starting inside the two gyres move on some invariant rings around the two oscillating centers located near $x = 0.5, 1.5$, $y = 0.5$. We expect that most of the initial conditions in these gyres belong to KAM tori, namely, they perform regular (quasiperiodic) motion. We observe that the properties of the fields $M^{mean}_{\mathbf{r}}, M^{shift}_{\mathbf{r}}$, $M^{\pm}_{\mathbf{r}}$ (Figs. 2(i)-2(l)), and their PDFs and CDFs in the CSs (Fig. 3) are similar to those of the steady gyres. To gain intuition, assume that the trajectories are of the form: $x(t;t_0) = x_c(t;t_0) + g(t;x_0)$

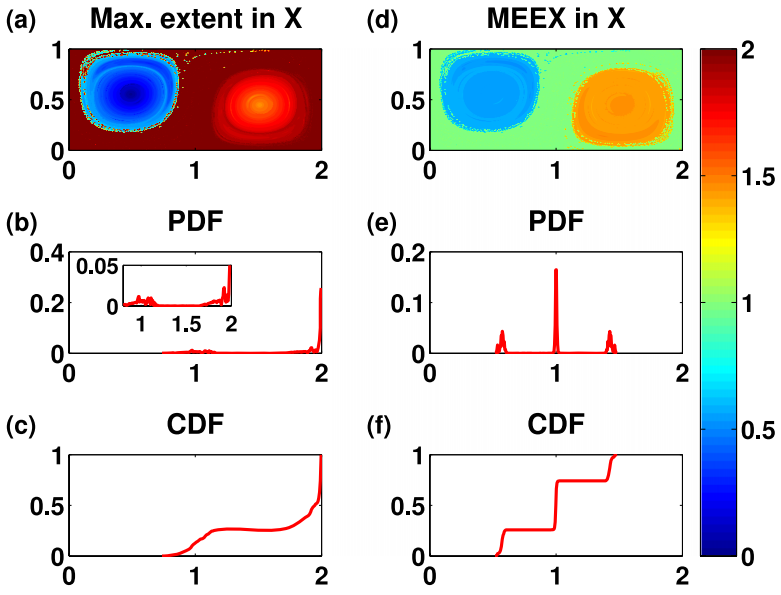

FIG. 3. Oscillatory double gyre—the maximal extent and the extremal mean in x: $M^{+}_{(1,0)}$, $M^{mean}_{(1,0)}$, their PDF, CDF. In the CDF of $M^{+}_{(1,0)}$, the two gyres appear as two parabolic segments starting near the x values 0.8 and 1.7 whereas the mixing layer appears as a sharp jump at $x = 2$, so these three structures are clearly distinguishable in this CDF, whereas in the PDF, the high concentration of the distribution function in the mixing layer bin ($x_{max} \lesssim 2$) makes the contributions to the regular coherent structures hardly detectable (see inset). In the CDF of $M^{mean}_{(1,0)}$, the two gyres and the mixing layer all appear as sharp jumps, so these three structures are distinguishable, yet their different character is not clearly identifiable. Equation (10), $A = \epsilon = 0.25$, $\omega = 2\pi/10$, and $\tau = 200$.

where $x_c(t;t_0)$ is some unknown slowly moving center and g is rapidly oscillating with zero mean (otherwise the particle drifts away from the center). The main difference between these and the stationary CSs, and in fact a way to identify these oscillating structures, appears when one examines the value of $M^{\pm}_{\mathbf{r}}$ at the coherent structure center $x_c(t;t_0)$, where, as before, we may define $x_c(t_0;t_0)$ as the trajectory along which $M_{\mathbf{r}}$ attains its local minima. In the steady case, we have $M^{-}_{\mathbf{r}} = M^{+}_{\mathbf{r}} = x_c(t_0;t_0)\cdot\mathbf{r}$, whereas in the oscillating case these values provide the minimal and maximal central location of the coherent structure along the $\mathbf{r}$ direction, see Figs. 2(i)-2(l) (see also Fig. 4).

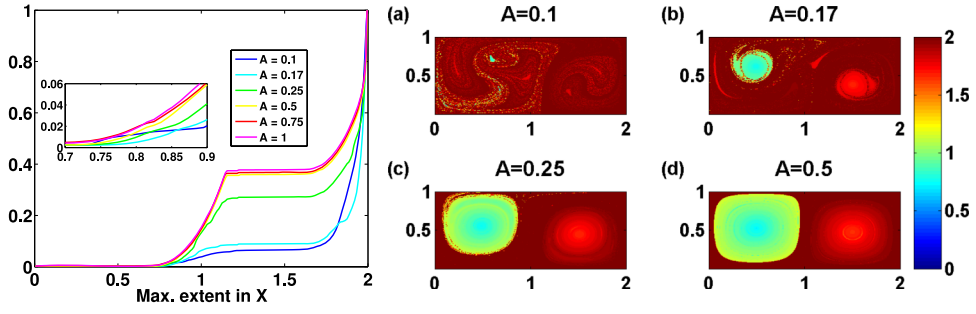

FIG. 4. MET field for the oscillatory double gyre for different base flow intensities A after 20 periods. Right: The maximal extent in x, $M^{+}_{(1,0)}$, is shown for four different base flow strengths. Left: The corresponding CDF for these and additional values of A. The CDF provides succinct presentation of the CSs size and location for the different flows without using any flow visualization analysis. The two gyres and the mixing layer are distinguishable: the left (respectively, right) gyre corresponds to the parabolic increase in the CDF starting near $x = 0.75$ (respectively, near $x = 1.7$) whereas the mixing layer corresponds to the sharp increase of the CDF near $x = 2$. The difference between the location of the gyre center and its maximal value provides information regarding its oscillation magnitude. The accumulated size of the coherent structures is seen to decrease here with decreasing A thus providing estimates for the area of the mixing zone. In all figures $\epsilon = 0.25$, $\omega = 2\pi/10$, and $t_1 = 0$, $\tau = 200$.

In the oscillatory case, a mixing layer appears: it consists of chaotic trajectories having sensitive dependence on i.c. that eventually encircle both gyres. Hence, for almost all i.c. x_0 in the mixing layer, the values of $M_{\mathbf{r}}^{shift}, M_{\mathbf{r}}^{\pm}, M_{\mathbf{r}}^{mean}$ asymptote to the width/the extent/the mean extent of the mixing layer in the **r** direction. It follows that the boundary between the mixing layer and the coherent structure in the MET fields plots is sharp—the MET are discontinuous at this boundary (Figs. 3–5). The PDFs of $M_{\mathbf{r}}^{shift}, M_{\mathbf{r}}^{\pm}, M_{\mathbf{r}}^{mean}$ converge to a delta function on the chaotic component, at the corresponding value of the shift/maximal/minimal/mean extent of the mixing layer (in the present case the maximal/minimal extent of the domain)—the chaotic bin. In the PDF of these fields, the only observable structure is the mixing layer whereas the regular coherent structures become invisible (Fig. 3(b)). In the CDF, the finite (i.e., non-infinitesimal) volume of the chaotic layer is apparent (Fig. 3(c)).

Fig. 4 demonstrates that the CDF of the MET field $M_{(1,0)}^{+}$ provides a succinct way to compare the mixing properties of different flow fields. In this figure, we compare the CDFs of the unsteady double gyre model, after 20 periods, for increasing power of the gyre intensity. By increasing the gyre intensity (A in Eq. (10)), we effectively decrease the non-dimensional period of the oscillatory component, bringing the system closer to the near-integrable regime.[25] The CDFs reveal how the two CS centers oscillate to larger extent and shrink in size as A is decreased without using any flow visualization analysis. Indeed, notice that the parabolic increase in the CDF starting near $x = 0.7$ ($x = 1.7$) corresponds to the maximal x-locations of the left (right) CS center, respectively. Thus, the change in this value with A (see inset) indicates that the centers experience larger oscillations as A decreases. The plateau value of the CDF provides the area of the left CS (seen to decrease from 40% of the area to nearly vanishing values as A decreases). The sharp increase in the CDF towards $x = 2.0$ indicates the transition to the mixing layer orbits, thus, for sufficiently large τ, the value of the CDF at the transition point provides the total fraction of area of the regular component. Notice that when A decreases to 0.17, the two gyres break into smaller CSs, some of these begin to rotate in the box (see the bright red crescent on the left part of the box—this crescent together with the island to the right of the center line corresponds to a period two CS. The large discrepancy between the location of this crescent and the $M_{(\mathbf{1},\mathbf{0})}^{+}$ value in it, which is equal to that found in the other island, suggests its rotational nature. This may be verified by trajectory computations and by looking at the minimal extent field, not shown).

1. Sensitivity tests to time dependence and particle density

Fig. 5 shows the MET field $M_{(1,0)}^{+}$ and its CDFs at several times, showing the convergence of the MET field to its asymptotic values which are constant on each ergodic component. It is seen that while the CDF component of the CSs appears to converge already after 5 periods, the mixing component has not reached its asymptotic form even after 40 periods. Namely, the convergence

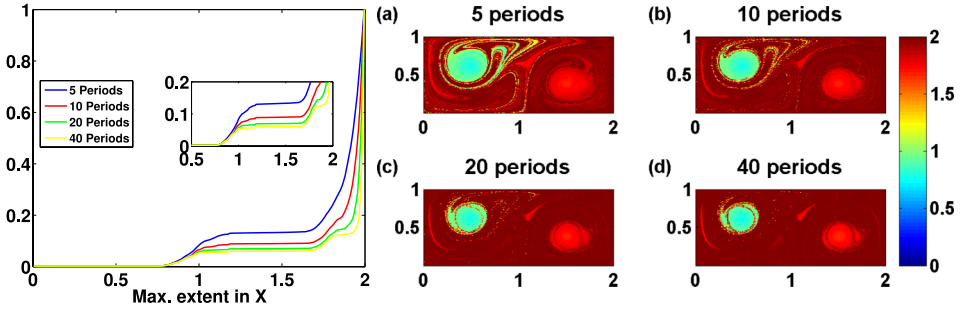

FIG. 5. MET fields for the oscillatory double gyre after 5 (a), 10 (b), 20 (c), and 40 (d) periods and their CDFs (left). The convergence of the CDFs and of the MET fields in regular regions is mainly achieved already after 5 periods, whereas the mixing layers have slower convergence and do not achieve their asymptotic behavior even after 40 periods. Here $A = 0.17$, $\epsilon = 0.25$, and $\omega = 2\pi/10$.

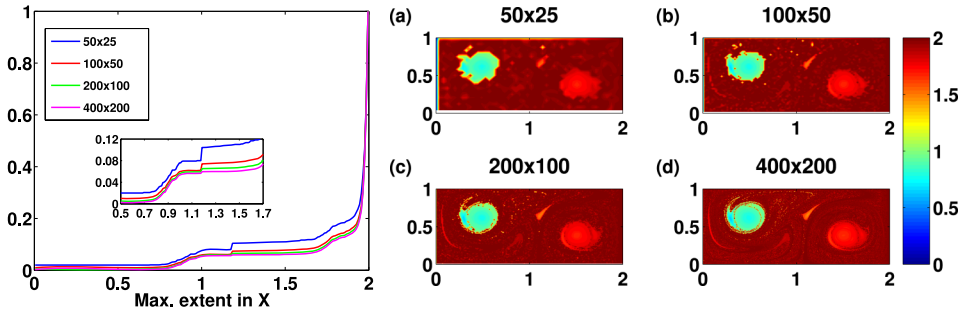

FIG. 6. Dependence on spatial resolution of the Maximal extent field and its CDFs. The number of particles is increased by a factor of 64 from (a) to (d). The fast convergence of the CDF becomes even more dramatic (the lowest 3 curves become indistinguishable, and the jump at $x = 1.2$ disappears) when the particles that are restricted to the rectangle boundaries are discarded. Here, $A = 0.17$, $\epsilon = 0.25$, and $\omega = 2\pi/10$, after 20 periods.

characteristics of these fields are different in the mixing vs. the CS regions. Indeed, high variability in the convergence time due to stickiness and long tails is expected to emerge in the chaotic zone whereas in the coherent structures, the convergence is expected to be regular for most i.c. Notice that the ghost of the stable manifold is readily seen for short extremal windows. These distinct convergence properties and the transient features of the MET may be utilized to distinguish between different regions and for locating dividing surfaces—this is left to future studies.

Fig. 6 shows the maximal extent in x and its CDF for 4 different spatial resolutions. The CDF converges rapidly as the resolution is increased. The spurious jump of the CDF at $x = 1.2$ which disappears with the increased resolution is associated with the boundary particles that remain on the rectangular boundary for all times and thus corresponds to an artificial effect caused by the choice of the grid. When these particles are discarded, one can hardly detect the difference between the four curves (not shown). Fig. 7 shows RD field for the same resolutions. The spurious patchiness of the RD at low resolutions is apparent—we observe that the small CS structures located near the domain center may be detected in the low resolution max extent plots (Figs. 6(a) and 6(b)) but not in the corresponding RD plots (Figs. 7(a) and 7(b)).

B. Coherent structures in open flows

Consider next an open flow model, the OVP: a vortex pair in an oscillating strain-rate field embedded in a uniform flow. The non-dimensional stream function[39] is of the form[51]

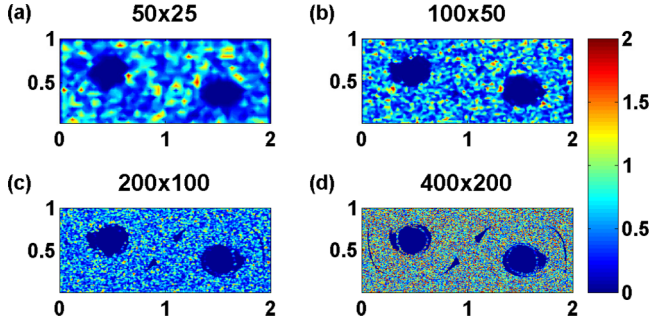

FIG. 7. Dependence on spatial resolution of the RD field. The same 4 resolutions as in Fig. 6 are used to calculated the RD field. The spurious patchiness at the two lowest resolutions (a) and (b) hides the existence of the small CS structures near $x = 1$—these do appear in the lowest resolution of the max extent plots Figs. 6(a) and 6(b). Here $A = 0.17$, $\epsilon = 0.25$, $\omega = 2\pi/10$.

$$\psi(x,y,t) = -\log\frac{(x-x_v)^2+(y-y_v)^2}{(x-x_v)^2+(y+y_v)^2} - v\,y + \epsilon x\,y\sin(\omega t)$$
$$\frac{dx_v}{dt} = \frac{1}{2y_v} - v + \epsilon x_v \sin(\omega t), \tag{11}$$
$$\frac{dy_v}{dt} = -\epsilon y_v \sin(\omega t),$$

where $(x_v(t), \pm y_v(t))$ denote the vortex locations and $x_v(0) = 0, y_v(0) = 1$. For $\epsilon = 0$, sufficiently far from the vortices, the particles move with a constant velocity $(-v, 0)$, whereas for non-zero ϵ these particles are also subjected to the oscillatory strain field. The vortex pair itself moves, in an oscillatory fashion, with an average horizontal velocity $v_{vort} = (0.5 - v + O(\epsilon), 0)$. As the vortex pair advects, it carries with it a body of fluid, namely, particles that move with the same averaged velocity v_{vort}, and due to the oscillations it sheds parts of this body of fluid in the form of lobes.[39] Originally, v was tuned so that $v_{vort} \approx 0$ and thus the mixing was observed in the vortex pair moving frame. Here, we take different values of v to examine the dependence of the MET methodology on the translational frame of reference.[52]

For negative v (respectively, large positive v, $v > 0.5 + O(\epsilon)$) all particles move to the right (respectively, to the left). The more complex behavior appears for small positive v ($0 < v < 0.5 + O(\epsilon)$), where the particles carried with the vortices move in the positive x direction, and the surrounding particles[53] move on average to the left.

To better understand the properties of the MET fields in such open flows, let us discuss the structure of trajectories in this flow. Trajectories moving with the vortex pair are of the form: $x(t;t_0) = v_{vort}(t - t_0) + x_c(t;t_0) + g(t;x_0)$ where $x_c(t;t_0)$ denotes a slow bounded motion of the vortex center and g denotes the bounded fast oscillating part of the trajectory around the vortex. Consider a general direction $\mathbf{r}$ and assume for now that $v_{vort} \cdot \mathbf{r} > 0$. Then, for sufficiently large $\tau + t_1$, $M^+_{\mathbf{r}}(\tau; x_0, t_1) \approx (v_{vort} \cdot \mathbf{r})(\tau + t_1 - t_0) + O(1)$, so all particles belonging to the CS associated with the vortex pair have a similar maximal extent.[54] Since we assumed here that the CS moves in the positive $\mathbf{r}$ direction, the minimal extent in direction $\mathbf{r}$ is essentially, up to some constant, given by the position of the particle at the beginning of the extremal window: $M^-_{\mathbf{r}}(\tau; x_0, t_1) \approx x(t_1; t_0) \cdot \mathbf{r}$. Hence, the $M^-_{\mathbf{r}}$ provides a meaningful characterization of the CS only for sufficiently large t_1, $M^-_{\mathbf{r}}(\tau; x_0, t_1) \approx (v_{vort} \cdot \mathbf{r})(t_1 - t_0) + O(1)$. Notice now that if the direction of the vortex pair motion reverses, so that $v_{vort} \cdot \mathbf{r} < 0$, the same conclusions apply with the roles of $M^+_{\mathbf{r}}$ and $M^-_{\mathbf{r}}$ exchanged. Taking the mean or difference of these two values $M^{mean}_{\mathbf{r}}(\tau; x_0, t_1) \approx (v_{vort} \cdot \mathbf{r})(\tau/2 + t_1 - t_0) + O(1)$ or $M^{shift}_{\mathbf{r}}(\tau; x_0, t_1) \approx (v_{vort} \cdot \mathbf{r})\tau + O(1)$ enables a meaningful characterization of CSs that move with different velocities in the direction $\mathbf{r}$ without the need to experiment with the extremal window starting location, t_1, and without the need to choose between maximal and minimal extents according to the CS direction of motion (allowing one to run the diagnostics without saving the full trajectories). This suggests that the $M^{mean,shift}_{\mathbf{r}}$ fields are more appropriate for detecting CS structures in open flows, and that using non-trivial extremal window helps in identifying the CSs. These arguments are expected to hold even when the CS velocity is not constant and is unknown, as long as the CS averaged motion in the direction $\mathbf{r}$ is unidirectional on the observational time scale and is distinguishable from its surroundings. If one chooses a direction $\mathbf{r}$ which is perpendicular to the direction of motion (e.g., the y direction here), the number of separate regions may be possibly detected (if $\mathbf{r}$ is resolving), but the information on the CS motion is lost. Below, we demonstrate these properties on the OVP model and in Sec. IV on real data.

Fig. 8 shows[55] the MEEX in x and the associated area-scaled CDFs for the OVP flow at several extremal windows of increasing lengths for $v = 0.25$, where particles move in both positive and negative directions. Here, and in general in the open flow setting, the size of the seeding area is arbitrary, and thus, instead of plotting the CDF we plot the accumulative area in the region, so that the CS area may be directly extracted from these plots, independently of the initial seeding region.

The CSs appear as a sharp increase in the CDF, its center moving with time. Thus, by following this sharp rise in the CDF, it is possible to detect the area and location of the body of fluid which advects with the vortices as well as to identify the volume of fluid that is shed by the lobes, see figure caption for specific examples.

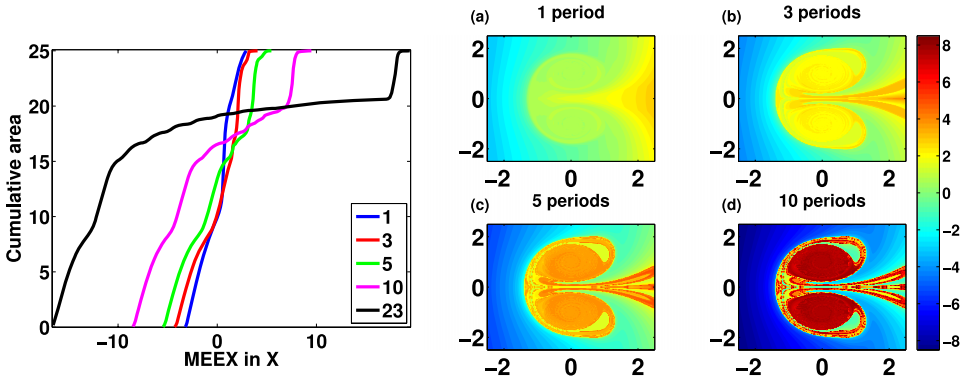

FIG. 8. The MEEX in x for the OVP open flow at $v = 0.25$—dependence on time. The four right panels show the MEEX in x, $M^{mean}_{(1,0)}$, at four different extremal windows ($t_1 = 0, \tau = (1, 3, 5, 10) \cdot 2\pi/\omega$) for the OVP flow (Eq. (11) with $\epsilon = 0.2, \omega = 1.45, v = 0.25$). The left panel shows the CDFs of this flow, multiplied by the area factor of the seeded domain, at the corresponding times—and, the rightmost curve, after 23 periods (see Fig. 9(c)). The location and size of the vortical core may be identified from the CDFs; the location of the core at different time points corresponds, roughly, to twice (recall that this is the **mean** of the extrema extents) the x value at which a sharp rise in the CDF occurs (e.g., after 10 periods the vortex is centered near $x = 15$). The area of the fluid carried by the vortices is estimated by the height of this sharp increase in the scaled CDF, namely, the area carried by the vortex after 10 periods is estimated to be ≈ 5. The area of the lobes that are shed from the vortex region corresponds to the small wiggles in the CDF. The monotone increase in the CDF up to the lobe shedding regime corresponds to the outer particles that move on average with negative horizontal velocities of approximately $-v$, with MEEX value of approximately $-v\tau/2 + x_0 + O(1)$.

Notice that for the OVP flow, trajectories that are far from the vortices experience, on average, a nearly uniform constant velocity. The MET fields have a nice smooth dependence on initial conditions in such regions. The CDFs thus have a bulk smooth region corresponding to the background flow, a quadratically increasing portion with a moving center that corresponds to the CS, and some shedding of lobes that appear as small steps in the CDF, see Figs. 8 and 9.

Fig. 9 (respectively, 10) shows the MEEX in x (respectively, in direction $\mathbf{r} = (1,4)$) of the OVP flow for different frequencies of the strain field oscillations. As expected, the CSs area depends non-monotonically on the frequency,[25] and this property is apparent from both the CDF diagram and the extremal field plots. While the MEEX in the x direction lumps together the two CSs associated with the two vortices, the $(1,4)$ direction resolves the two structures.

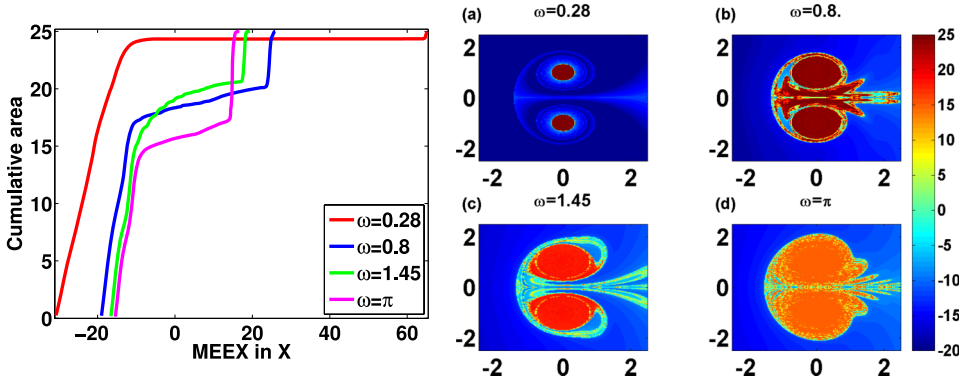

FIG. 9. The CSs dependence on the strain field frequency. On the right panels the MEEX in x, $M^{mean}_{(1,0)}$, is shown for four different frequencies at $t_1 = 0, \tau = 100$ (about 5, 12, 23, and 50 periods of the corresponding frequencies, notice that in panel (a) the colorbar does not include the extreme, see the CDF for the actual values). The left panel shows the CDF of these fields. The area of the CSs is approximately given by the height of the sharp increased part (i.e., the areas are approximately 7, 5, 5.5, 0.5 for $\omega = \pi, 1.45, 0.8, 0.28$, respectively). The location is given approximately by double the position of this sharp increase (since we plot the mean and the minimal value here is approximately zero), namely, $x_c \approx 30, 35, 50, 135$, respectively. The non-monotone dependence of the core area on ω is apparent.

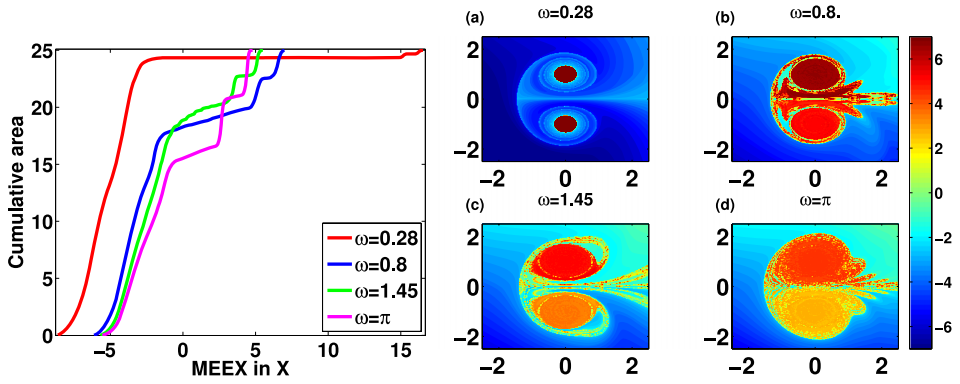

FIG. 10. CSs in a resolving direction. On the right panel, the MEEX fields in direction (1, 4), $M^{mean}_{(1,4)}$, are shown for the four different frequencies shown in Fig. 9 (again (a) suffers from the colorbar cutoff). The left panel shows the CDF of these fields. Here, the resolving direction distinguishes between the lower and upper vortex CSs, showing, for example, that they are of equal areas.

1. Sensitivity tests to extremal windows and different translational reference frames

Fig. 11 compares the different MET quantifiers for three extremal windows. We see that the MEEX field is non-degenerate, whereas the maximal/minimal fields are degenerate at $t_1 = 0$ (left-most and right-most columns). Thus, while the MEEX and the shift fields with $t_1 = 0$ reveal

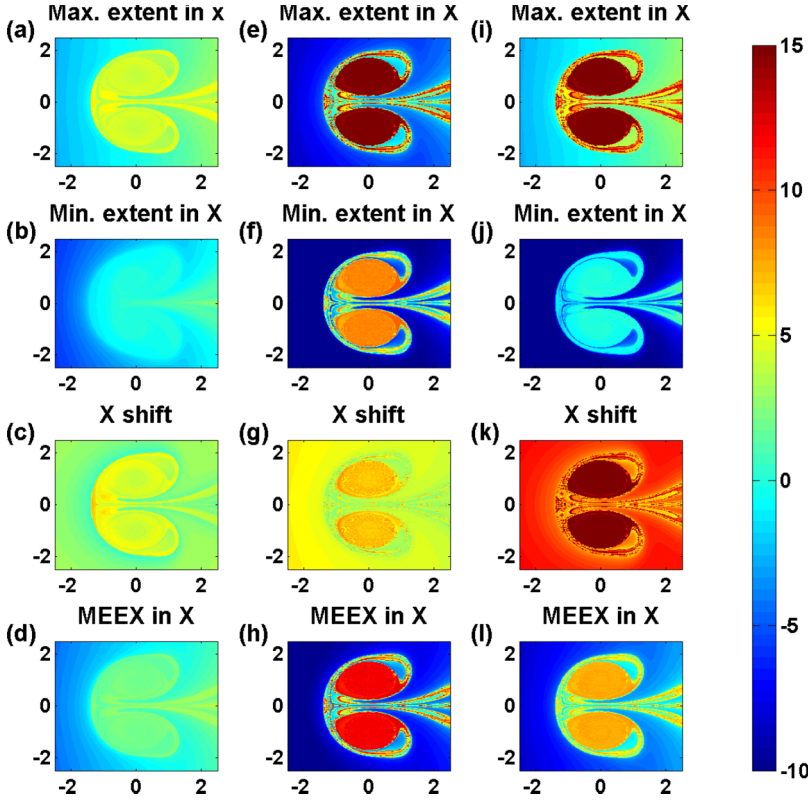

FIG. 11. The four different MET quantifiers for three different extremal windows: (a)-(d) a 3 periods window starting at $t_1 = 0$, (e)-(h) 3 period window starting at $t_1 = 7(2\pi/\omega)$, (i)-(l) 10 period window starting at $t_1 = 0$. For $t_1 = 0$, (left and right columns) the maximal/minimal extent fields cannot characterize left/right moving trajectories, respectively, whereas the MEEX and shift neutralize this effect. Taking a large t_1 makes the maximal/minimal/mean fields quite similar and resolves this problem (middle column).

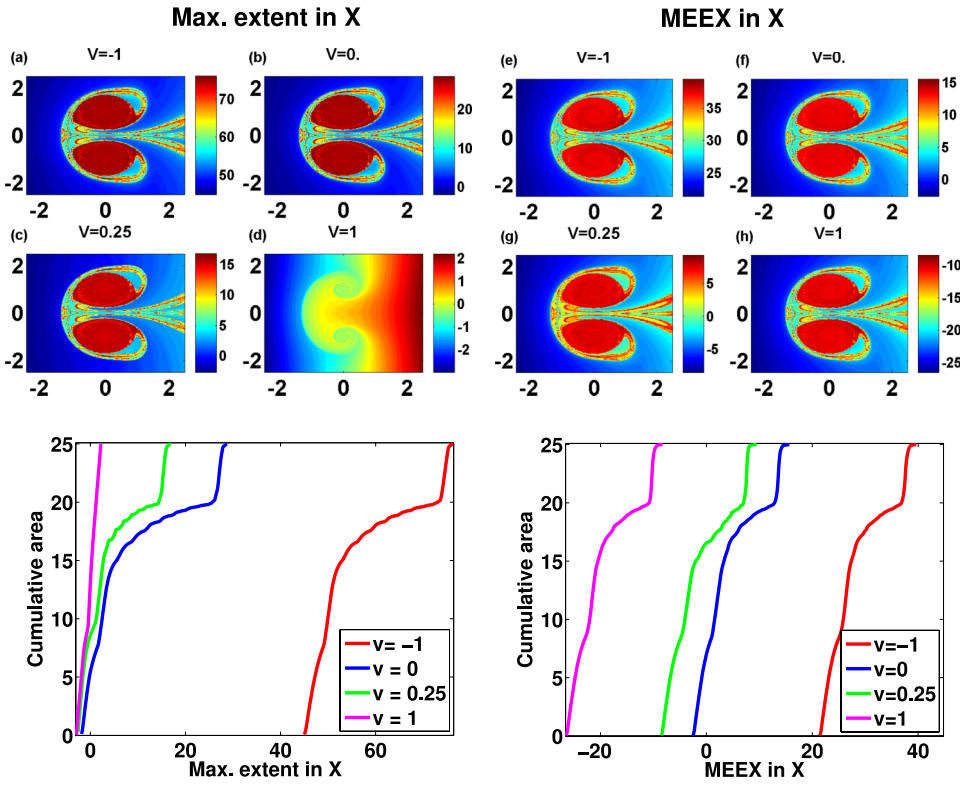

FIG. 12. The MET dependence on translational frame of reference. The OVP flow with the same parameters as in Fig. 8 after 10 periods in four different translational moving frames (Eq. (11) with $\epsilon = 0.2$, $\omega = 1.45$, and $v = -1, 0, 0.25, 1$ at $\tau = 10\frac{2\pi}{\omega}$). At $v = 0.25$ and $v = 1$ a large portion of i.c. moves to the left, the maximal extent for these i.c. is simply their initial horizontal positions, and hence the CDF of the maximal extent does not reflect inherent features of the flow. For $v = -1$, all i.c. move eventually to the right and the CDF of the max extent field and of the MEEX, stretched by a factor of two, is identical. Due to this property, we see that the MEEX CDF has a much weaker dependence on v than the maximal extent CDF.

the mixing pattern even after 3 periods (left column), and more so after 10 periods (right column), the maximal/minimal extents remain with the same initial degeneracy. On the other hand, when we take t_1 to be sufficiently large, these degeneracies lift, and the maximal/minimal extent fields supply similar information as the MEEX.

Fig. 12 shows the MEEX and the maximal extent in x of the OVP flow for different moving frame velocities, v. While the MEEX field appears to be quite insensitive to the value of v (though some peculiarities appear at $v = 0.25$), the maximal extent field with $t_1 = 0$ has strong v dependence—the regions in which it records only the initial positions or initial oscillations of the left moving particles depend on v (Figs. 12(c) and 12(d)). Thus, it is suggested that the MEEX and the shift fields are insensitive to monotonic translations and applicable even when some structures move out of the original region in which the particles are seeded in opposite directions. On the other hand, the maximal/minimal extent fields provide meaningful information only if one shifts the extremal window sufficiently far from the origin or if all trajectories happen to move in the positive/negative **r**-direction, respectively. Note that these features are especially relevant to geophysical applications in which the observed domain is open and there is an unknown underlying current, see Sec. IV.

We conclude that in the open flow settings it is advantageous to use the MEEX, the mean of the extrema extents in a direction that is both resolving and not perpendicular to the CS averaged velocity. If the observation time is sufficiently long, it is preferable to use non-trivial extremal windows, and in this case the MEEX, the maximal, and the minimal extents provide similar information (in fact, the comparison may provide a way to check the suitability of the extremal window). Following

the changes in the CDFs of the various MET fields in different directions, the CS approximate location, size, and averaged velocity may be estimated.

IV. REAL DATA

We next apply the MET analysis to real data from the South Atlantic, in the region shown in Fig. 13, using surface currents obtained from the AVISO database (www.aviso.oceanobs.com). Transport and identification of CSs in this region during this period were studied before.[56,57] As in Ref. 57, our analysis suggests fewer CSs than identified, e.g., by the Okubo-Weiss criterion or by the method of Ref. 35. One of the CSs we identify (A in Figs. 14 and 15) was identified by Ref. 57 while the rest are undetermined. Within this velocity field we deploy 80 000 virtual particles on an approximately 4 km grid (approximately 3.6 km in longitude and 4.4 km in latitude) and track them for 90 consecutive days starting on November 24, 2006.

During the period examined in this study, the distributed global product was a combination of altimetric data from Jason-1 and -2 and Envisat missions. The dataset is comprised of weekly near-real-time sea-level-anomaly data files, gridded on a $\frac{1}{3}^\circ \times \frac{1}{3}^\circ$ Mercator grid. The methodology for extracting a velocity field from sea level data is known to introduce errors, as does the linear interpolation scheme we use for integrating trajectories. Other sources of uncertainties in the data are due to tides and atmospheric conditions. In particular, the extracted velocity field is not area-preserving. Although in stratified ocean the flow is approximately 2D (i.e., vertical velocities are few orders of magnitude smaller than the horizontal velocities), 3D effects may qualitatively change surface mixing.[44] We calculate the MET on a cartesian grid, with the origin set at the South-West corner (34°*S*, 4°*W*), recording the results every hour. This introduces additional error due to the convergence of longitudes on the spherical Earth, which, for this latitude belt, is up to 5% error, smaller than the above-mentioned errors. Despite these errors and limitations, as shown below, our analysis captures the existing CSs.

Since we do not have *a priori* knowledge of the flow field structure, and in particular of its resolving directions, we calculate various MET characteristics along both the zonal (X, longitudinal, Figs. 14, 16, and 17) and meridional (Y, latitudinal, Fig. 18 left panel) directions for a few extremal time windows. As might be expected, we find that the X direction better resolves the CSs in this region due to their westward propagation. In Fig. 14, we present the MEEX in X (top row), the maximal extent in X (middle row), and the minimal extent in X (lower row) for a few extremal time windows (columns from left to right): 0-30, 30-60, 60-90, and 0-90 days. Compared with the Okubo-Weiss field shown in Fig. 13, fewer CSs exist, as previously discussed.[57]

From the leftmost and rightmost columns, it is clear that the MEEX captures the CSs better than the maximal extent in X, as in the OVP toy model example. The reason is clear: in this case, the CSs migrate mainly westward, hence the maximal extent in X basically records the initial conditions of trajectories. Since particles move both eastward and westward, once an interim window is

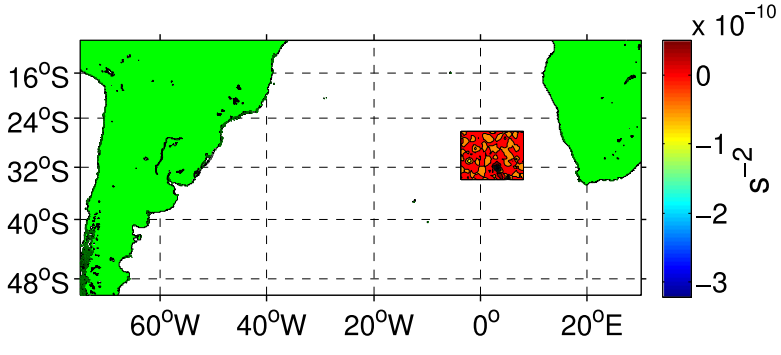

FIG. 13. The South Atlantic region in which particles are seeded on November 24, 2006 is the colored rectangular domain. The colors represent the Okubo-Weiss field (showing some spurious structures[57]) for November 22, 2006, the closest date to November 24, 2006 for which raw data from the AVISO data set are available.

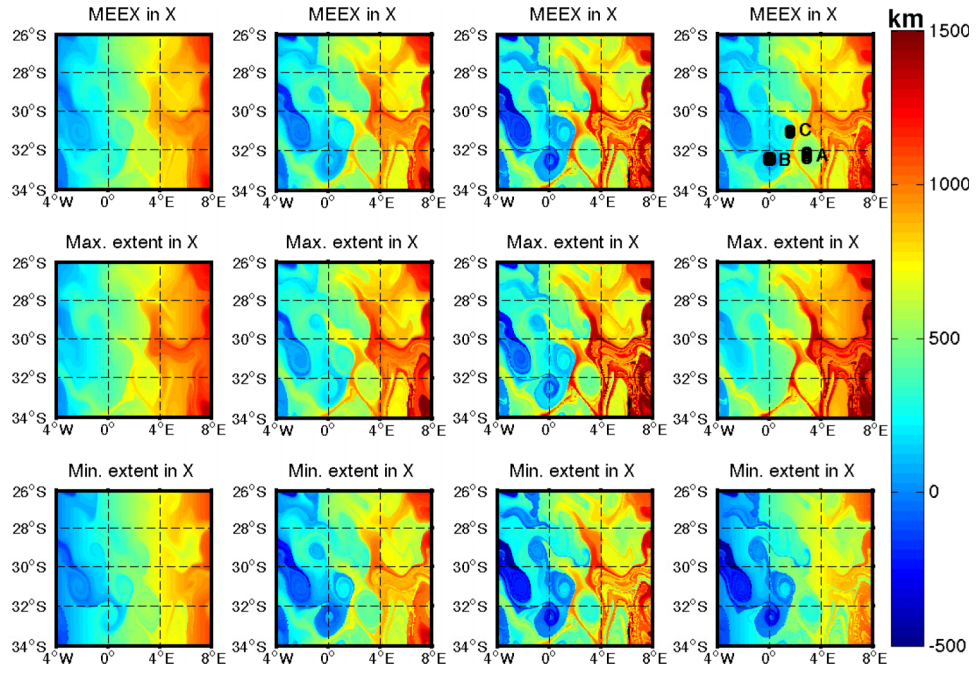

FIG. 14. MEEX in X (top row), maximal extent in X (middle row), and minimal extent in X (lower row) for a few extremal time windows (columns from left to right): 0-30, 30-60, 60-90, and 0-90 days. The particles were seeded on November 24, 2006. Several separate CSs are identified. The three black dotted groups, marked by A-C in the upper-right panel, represent the initial positions of the particle trajectories shown in Fig. 15.

selected, as in the 2nd and 3rd columns, the CSs are seen in all MET fields, including the maximal extent.

Notice that the MEEX field provides information regarding the location and the motion of the CSs. Take, for example, the main CS centered at (32.5°S, 3°E), labeled as (A) in Figs. 14 (top-right panel) and 15. We observe that the initial location in X of this CS is at X = 770 km (seen, for example, from the middle row-right most or left most columns) whereas the MEEX field value at this CS after 90 days is at about X = 500 km (top-right panel), hence the CS moved westward at about double the difference, namely, about 550 km, i.e., about 5°. This is nicely verified by trajectory integration in Fig. 15. See also Fig. 17 showing, via CDF plots, the westward propagation of this CS in time.

Numerous CSs appear in the large seeded region (26° – 34°S, 4°W – 8°E, over million km^2) and the PDF and CDF of any of the MET characteristics, in both the X and Y directions, lump together many CSs in such a large region. Hence, as expected, these figures cannot be used to detect

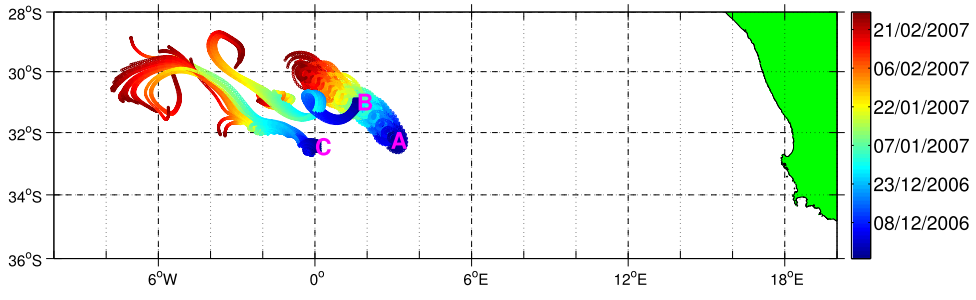

FIG. 15. Trajectories of particles seeded within regions identified as CSs from the MEEX in X field (Fig. 14, top-right panel). The colors represent their locations at the indicated dates. The existence of the diagnosed CSs at these locations and their westward propagation is clearly seen.

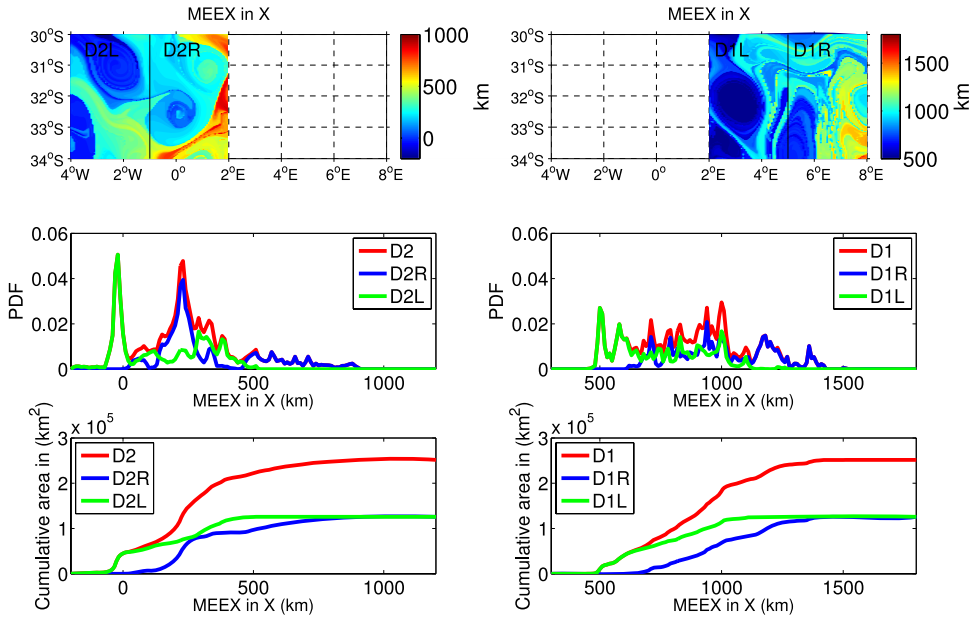

FIG. 16. MEEX in X for 0-90 days (upper row), PDF (middle row), and CDF (lower row) for different regions and sub-regions of the latitude belt $30° - 34°S$. Right column: regions D1 ($2°E - 8°E$, red), and its sub-regions D1L ($2°E - 5°E$, green), and D1R ($5°E - 8°E$, blue). Left column: region D2 ($4°W - 2°W$), red), and its two sub-regions D2L ($4°W - 1°W$, green), and D2R ($1°W - 2°E$, blue). The upper row shows sub-regions of Fig. 14 top-right panel in the regional colorbar.

CSs. To identify the location and size of the CSs in the large domain we subdivide it to smaller sub-domains, plot the PDF and CDF for each one of them aiming to identify isolated structures. Fig. 16 shows the MEEX in X (upper row), PDF of the MEEX in X (middle), and CDF (lower row) for the latitudinal belt $30° - 34°S$ subdivided to two main sub-domains, each of these is again subdivided to two (see caption). By subdividing the two domains and inspecting the PDF, it is possible to identify when there is possibly only one CS in a domain: this occurs when there is a dominant peak in which the PDF of one of the sub-domains is the main contributor to the corresponding peak of the large domain. We then suspect that an isolated CS exists in the specific sub-domain. For example, the overlapping of the green and red line in the left-most peak on the left middle panel of Fig. 16 is clearly identified with the CS centered initially at $(31°S, 2.5°W)$. As in the above examples, the shape of the CDF provides an estimate for the size and location of the CS.

The time-dependence of the CDF for the sub-domain D1L is shown in Fig. 17. The locations of the first rise of the CDFs at the sequence of the extremal windows move to the left, indicating that

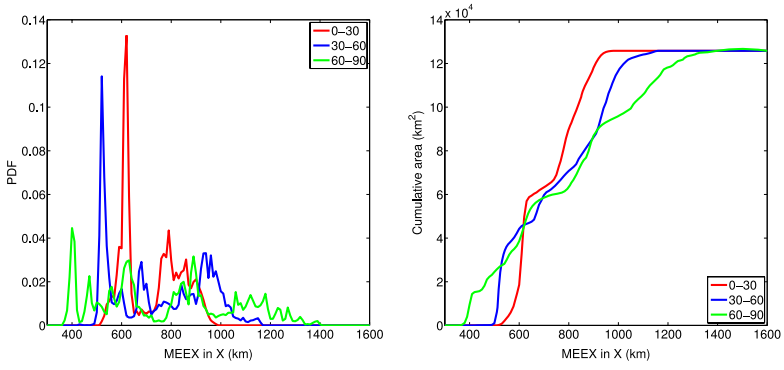

FIG. 17. The PDF and CDF of the MEEX in longitudinal direction—dependence on time for region D1L. The creation and motion of CS in this region are observed (see text).

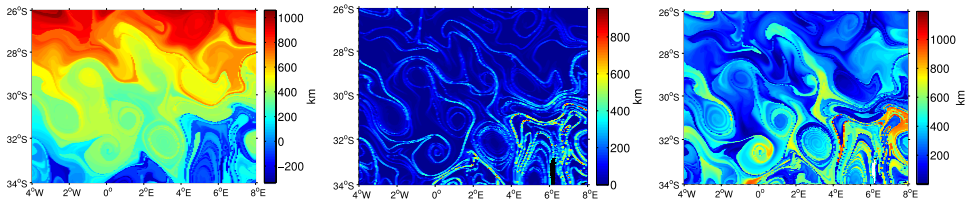

FIG. 18. Additional Lagrangian diagnostics: MEEX in Y (left), relative dispersion (middle), and absolute dispersion (right) for 0-90 days.

the CS propagates westward. The heights of the this first rise become lower, indicating that this CS is shrinking in size.

Fig. 18 shows a few more fields that are often used to identify CSs. The left panel shows the MEEX in latitude—we see that many of the CSs have similar MEEX in y value. This reflects the observation that these structures are mostly aligned along latitudinal belts, moving to the north-west essentially together. The RD and AD fields are also plotted (middle and right panels). Not surprisingly, in all these fields, the same patterns emerge.

V. DISCUSSION

Our main result is the introduction of a new family of Lagrangian diagnostics, in particular the MET, and the demonstration that the CDF of the MET allows one to find important characteristics of the CSs at low computational cost. In particular, the number, location, and size of the CSs (nested sets of a continuum of ergodic components) with a volume above a threshold value may be found with no need for minimization or image processing procedures. A major advantage is thus the ability to compress a large amount of data into a simple diagnostic plot.

The computation of the MET is based on a single particle integration with no need for integrating derivatives or tracking sufficiently close-by neighbors. This suggests that such a method is easier and cheaper to utilize on sparsely seeded domains, yet a thorough study of its efficiency has not been conducted yet.

The signature of a CS in the CDF appears as a smooth curved increasing segment—the base of it and the value where it flattens or abruptly increases provide information on the CS spatial location and width along the specific direction that is used to compute the MET. The height difference between these values provides its area. The signature of a mixing layer (in closed domains) is a fast growing segment that asymptotes as τ, the extremal window, grows to infinity, to a discontinuity of the CDF. A motion of the CS corresponds to a shift of its corresponding segment in the CDF of the appropriate MET characteristic with hardly any change of its shape. We demonstrated that the MET provides insightful information using toy models in both closed and open domains and on a real data set from the South Atlantic.

The MET and many other Lagrangian quantifiers (such as RD, FTLE, the hypergraph map, and other averaged quantifiers[2,3,17,26,27,36]) have a common feature: asymptotically, these converge to constants on ergodic sets and hence, in principle, may be utilized to divide the phase space to separate ergodic components. In many applications, the transient properties of these and other Lagrangian quantifiers were studied, showing that in some cases, ridges of finite time realizations of these fields provide good predictors for dividing surfaces. We expect that similar analysis can also be applied to finite time realizations of extremal fields (see especially Figs. 5 and 8) and this direction has yet to be explored. Here, we exploit the asymptotic features of these fields as a way to identify CS. In this aspect, we note that the RD and FTLE are degenerated—they asymptote to zero in the regular regime and to a positive constant in the mixing zone. On the other hand, the value of the MET (and of the hypergraph map and other Lagrangian averages[3]) asymptotes to a smooth function in a regular region and to a constant in the chaotic zone. The unique feature of the MET is that if the direction $\mathbf{r}$ is resolving, its CDF readily provides additional information on the

location and number of CSs (whereas with the other quantifiers the CDF lumps together all coherent structures).

Another distinguishing characteristic of the MET is that the convergence to its asymptotic value is always monotone in time whereas in all other quantifiers, convergence to their asymptotic values is oscillatory (except the arc-length map[37,38] which is monotone yet unbounded). Hence, we expect that the convergence of the MET will be faster and more regular. In fact, the temporal convergence properties of the MET may be related to the universal convergence associated with extreme value statistics of ergodic dynamical systems.[46–50] The implications of these on the convergence of the CDF, on the spatial smoothness of the MET, and on the sensitivity of these to noise and velocity errors have yet to be investigated.

The MET fields are well suited for studying open flows. We demonstrated that in the real data example much information on the location, size, and propagation of the CSs may be gained by observing the MEEX field, by observing the MET fields on nontrivial extremal windows, by examining several directions, and by examining PDFs and CDFs of these on sub-domains.

The current work leaves many additional directions to be explored in future studies, including: (1) The transient MET fields in the CSs are quite smooth whereas their transient behavior in the mixing layers is noisy. This property may be utilized to distinguish between these regions on short time scales. More generally, the study of the transient behavior of the MET in τ,t_1 may reveal the structure (e.g., local dimension[36,48]) of the ergodic component. Possibly, it may reveal other transient transport processes, such as dividing surfaces and the lobe structure.[43] (2) The applications shown here suggest that additional insight may be obtained by studying the temporal and spatial dependence of extreme values of other observable functions in systems with mixed phase space (e.g., velocities, speed, distance from the origin, stretching rates, strain rates, FTLE, recurrences[48]). (3) The study of open flows needs to be further explored, in particular, the distinction between CSs, shear layers, and hyperbolic structures and their forms in the PDFs and CDFs of the various MET fields has not been studied yet. We also note that for open flows with moving CSs the difference between the traditional AD field and the MET fields is not dramatic, yet the MET fields provide the additional advantage of directional information and non-oscillatory convergence. Possibly, one may also study directional AD and RD fields and compare these to the MET. (4) In real applications, we often have a limited sampling of the flow along specific directions, e.g., by few drifters. How much of the flow characteristics can be extracted from such limited information is unclear. Based on our preliminary results (not shown), 1D sections might suffice to provide many of the flow characteristics. Moreover, this approach may work in higher dimensions as well. (5) In flows with a large number of CSs of different scales and locations, such as 2D-turbulent flows, it may become difficult to find resolving directions. In such cases, it may be beneficial to adopt a multiscale strategy by which resolving directions are sought on sub-domains. Preliminary results along this line are shown in Figs. 16 and 17, where one can see the promise (the appearance of nice isolated peaks in PDFs of small sub-domains) and some of the associated problems (e.g., how to distinguish between isolated peaks and noise and how to identify structures that are not CSs). One may envision an algorithmic approach by which the PDFs of different MET characteristics (MEEX in several directions, all MET fields on several extremal windows, calculation of these on several sub-domains) are compared to identify CSs more precisely. (6) Finally, we note that many of the above issues may be studied first on chaotic maps with mixed phase space behavior (e.g., we currently study the standard map and its higher dimensional extensions continuing, in some sense, a previously suggested approach for studying these maps[45]). Such studies allow for the introduction of a more rigorous mathematical analysis.

When compared with methods based on Eulerian data for eddy detection,[33–35] the Lagrangian diagnostics have a few advantages: (1) These can possibly be used to identify various kinds of CS, not necessarily eddies. (2) They are applicable for a wide range of scales, not just meso-scale structures dominated by vorticity. (3) Methods that rely on velocity derivatives, such as the Okubo-Weiss parameters, introduce noise to the data, especially when errors in the velocity field are not small when compared to the high spatial resolution. The identification of CS based on the computation of trajectories seems to be less sensitive to data errors.[58] In recent years, various

sophisticated Lagrangian diagnostics have been proposed.[3,14–17,26,30,36,37,41,59–61] One may envision a quick screening using the MET approach combined with some of these high-end methods.

In conclusion, we present new, promising Lagrangian diagnostics that enable the extraction of properties of coherent structures from large data sets by looking at extremal values of observables, their PDFs, and CDFs. These diagnostics are not only simple, intuitive, and computationally cheap; they also can potentially enable a significant data reduction, since it is possible to extract from the cumulative distribution functions much of the relevant information regarding the existence, location, size, and motion of the coherent structures.

ACKNOWLEDGMENTS

We thank the referees for the thorough reviews and insightful comments that had greatly contributed to improving the manuscript. We thank Dimitry Turaev for useful comments and suggestions. This study was supported by a grant from the Israel Science Foundation (to VRK) and by a grant from the Israeli Ministry of Science and Technology and the Taiwan Ministry of Science and Technology (to HG and EF). This work was stimulated from the M.Sc. thesis of Rotem Aharon.[43,44]

[1] G. Gawarkiewicz, S. Monismith, and J. Largier, "Observing larval transport processes affecting population connectivity progress and challenges," Oceanography **20**, 40–53 (2007).
[2] A. E. BozorgMagham, S. D. Ross, and D. G. Schmale III, "Real-time prediction of atmospheric Lagrangian coherent structures based on forecast data: An application and error analysis," Phys. D **258**, 47–60 (2013).
[3] I. Mezic, S. Loire, V. A. Fonoberov, and P. Hogan, "A new mixing diagnostic and gulf oil spill movement," Science **330**, 486–489 (2010).
[4] M. J. Olascoaga and G. Haller, "Forecasting sudden changes in environmental pollution patterns," Proc. Natl. Acad. Sci. U. S. A. **109**, 4738–4743 (2012).
[5] T. Peacock and G. Haller, "Lagrangian coherent structures: The hidden skeleton of fluid flows," Phys. Today **66**(2), 41–47 (2013).
[6] A. Melsom, F. Counillon, J. H. LaCasce, and L. Bertino, "Forecasting search areas using ensemble ocean circulation modeling," Ocean Dyn. **62**, 1245–1257 (2012).
[7] F. d'Ovidio, J. Isern-Fontanet, C. Lopez, E. Hernandez-Garcia, and E. Garcia-Ladona, "Comparison between Eulerian diagnostics and finite-size Lyapunov exponents computed from altimetry in the Algerian basin," Deep Sea Res., Part I **56**, 15–31 (2009).
[8] A. J. Mariano, A. Griffa, T. M. Özgökmen, and E. Zambianchi, "Lagrangian analysis and predictability of coastal and ocean dynamics 2000," J. Atmos. Oceanic Technol. **19**, 1114–1126 (2002).
[9] H. Aref, "The development of chaotic advection," Phys. Fluids **14**, 1315–1325 (2002).
[10] J. Ottino, *The Kinematics of Mixing: Stretching, Chaos, and Transport* (Cambridge University Press, Cambridge, MA, 1989).
[11] A. M. Mancho, D. Small, and S. Wiggins, "A tutorial on dynamical systems concepts applied to Lagrangian transport in oceanic flows defined as finite time data sets: Theoretical and computational issues," Phys. Rep. **437**, 55–124 (2006).
[12] F. J. Beron-vera and M. J. Olascoaga, "An assessment of the importance of chaotic stirring and turbulent mixing on the west Florida shelf," J. Phys. Oceanogr. **39**, 1743–1755 (2009).
[13] K. V. Koshel and S. V. Prants, "Chaotic advection in the ocean," Phys.-Usp. **49**, 1151–1178 (2006).
[14] T. Peacock and J. Dabiri, "Introduction to focus issue: Lagrangian coherent structures," Chaos **20**, 017501 (2010).
[15] E. M. Bollt and N. Santitissadeekorn, *Applied and Computational Measurable Dynamics, Mathematical modeling and computation* (SIAM, 2013).
[16] S. V. Prants, "Dynamical systems theory methods to study mixing and transport in the ocean," Phys. Scr. **87**, 038115 (2013).
[17] M. Budišić, R. Mohr, and I. Mezić, "Applied koopmanism," Chaos **22**, 047510 (2012).
[18] A. C. Poje and G. Haller, "Geometry of cross-stream mixing in a double-gyre ocean model," J. Phys. Oceanogr. **29**, 1649–1665 (1999).
[19] G. Haller and F. J. Beron-Vera, "Coherent Lagrangian vortices: The black holes of turbulence," J. Fluid Mech. **731**, R4 (2013).
[20] R. Pierrehumbert, "Tracer microstructure in the large-eddy dominated regime," Chaos Solitons Fractals **4**, 1091–1110 (1994).
[21] Z. Lin, J.-L. Thiffeault, and C. R. Doering, "Optimal stirring strategies for passive scalar mixing," J. Fluid Mech. **675**, 465–476 (2011).
[22] J. Lingevitch and A. Bernoff, "Advection of passive scalar by a vortex couple in the small-diffusion limit," J. Fluid Mech. **270**, 219–249 (1994).
[23] G. Mathew, I. Mezic, and L. Petzold, "A multiscale measure for mixing," Phys. D **211**, 23–46 (2005).
[24] D. Beigie, A. Leonard, and S. Wiggins, "A global study of enhanced stertching and diffusion in chaotic tangles," Phys. Fluids A **3**, 1039–1050 (1991).
[25] V. Rom-Kedar and A. Poje, "Universal properties of chaotic transport in the presence of diffusion," Phys. Fluids **11**, 2044–2057 (1999).

[26] G. Haller and G. Yuan, "Lagrangian coherent structures and mixing in two-dimensional turbulence," Physica D **147**, 352–370 (2000).
[27] S. C. Shadden, F. Lekien, and J. E. Marsden, "Definition and properties of Lagrangian coherent structures from finite-time Lyapunov exponents in two-dimensional aperiodic flows," Phys. D **212**, 271–304 (2005).
[28] S. Orre, B. Gjevik, and J. H. LaCasce, "Characterizing chaotic dispersion in a coastal tidal model," Cont. Shelf Res. **26**, 1360–1374 (2006).
[29] G. Boffetta, G. Lacorata, G. Radaelli, and A. Vulpiani, "Detecting barriers to transport: A review of different techniques," Phys. D **159**, 58–70 (2001).
[30] B. Lipphardt, D. Small, A. Kirwan, S. Wiggins, K. Ide, C. Grosch, and J. Paduan, "Synoptic Lagrangian maps: Application to surface transport in Monterey Bay," J. Mar. Res. **64**, 221–247 (2006).
[31] A. Okubo, "Horizontal dispersion of floatable particles in vicinity of velocity singularities such as convergences," Deep-Sea Res. Oceanogr. Abstr. **17**, 445–452 (1970).
[32] J. Weiss, "The dynamics of enstrophy transfer in 2-dimensional hydrodynamics," Phys. D **48**, 273–294 (1991).
[33] C. Dong, F. Nencioli, Y. Liu, and J. C. McWilliams, "An automated approach to detect oceanic eddies from satellite remotely sensed sea surface temperature data," Geosci. Remote Sens. Lett., IEEE **8**, 1055–1059 (2011).
[34] F. Nencioli, C. Dong, T. Dickey, L. Washburn, and J. C. McWilliams, "A vector geometry-based eddy detection algorithm and its application to a high-resolution numerical model product and high-frequency radar surface velocities in the southern california bight," J. Atmos. Oceanic Technol. **27**, 564–579 (2010).
[35] D. B. Chelton, M. G. Schlax, and R. M. Samelson, "Global observations of nonlinear mesoscale eddies," Prog. Oceanogr. **91**, 167–216 (2011).
[36] I. Rypina, S. E. Scott, L. J. Pratt, and M. G. Brown, "Investigating the connection between complexity of isolated trajectories and Lagrangian coherent structures," Nonlinear Processes Geophys. **18**, 977–987 (2011).
[37] C. Mendoza and A. M. Mancho, "Hidden geometry of ocean flows," Phys. Rev. Lett. **105**, 038501 (2010).
[38] C. Alvaro de la, C. Mechoso, A. Mancho, E. Serrano, and K. Ide, "Isentropic transport within the antarctic polar-night vortex: Rossby wave breaking evidence and Lagrangian structures," J. Atmos. Sci. **70**, 2982–3001 (2013).
[39] V. Rom-Kedar, A. Leonard, and S. Wiggins, "An analytical study of transport, mixing and chaos in an unsteady vortical flow," J. Fluid Mech. **214**, 347–394 (1990).
[40] M. Dellnitz and O. Junge, "On the approximation of complicated dynamical behavior," SIAM. J. Numer. Anal. **36**, 491–515 (1999).
[41] G. Froyland, K. Padberg, M. H. England, and A. M. Treguier, "Detection of coherent oceanic structures via transfer operators," Phys. Rev. Lett. **98**, 224503 (2007).
[42] G. Froyland and K. Padberg-Gehle, "Finite-time entropy: A probabilistic approach for measuring nonlinear stretching," Phys. D **241**, 1612–1628 (2012).
[43] R. Aharon, "Surface mixing induced by simple three dimensional flows," Master's thesis (Weizmann Institute of Science, Rehovot, Israel, 2009, available at http://www.earth.huji.ac.il/data/File/gildor/Rotem_thesis.pdf.
[44] R. Aharon, V. Rom-Kedar, and H. Gildor, "When complexity leads to simplicity: Ocean surface mixing simplified by vertical convection," Phys. Fluids **24**, 056603 (2012).
[45] R. Easton, J. Meiss, and S. Carver, "Exit times and transport for symplectic twist maps," Chaos **3**, 153–165 (1993).
[46] P. Collet, "Statistics of closest return for some non-uniformly hyperbolic systems," Ergodic Theory Dyn. Syst. **21**, 401–420 (2001).
[47] M. P. Holland, R. Vitolo, P. Rabassa, A. E. Sterk, and H. W. Broer, "Extreme value laws in dynamical systems under physical observables," Phys. D **241**, 497–513 (2012).
[48] V. Lucarini, D. Faranda, and J. Wouters, "Universal behaviour of extreme value statistics for selected observables of dynamical systems," J. Stat. Phys. **147**, 63–73 (2012).
[49] A. C. M. Freitas and J. M. Freitas, "On the link between dependence and independence in extreme value theory for dynamical systems," Stat. Probab. Lett. **78**, 1088–1093 (2008).
[50] J. M. Freitas, "Extremal behaviour of chaotic dynamics," Dyn. Syst: Int. J. **28**, 302–332 (2013).
[51] Remark: In the dimensional units (see Ref. 39, Eq. (2.1)-(2.4)): $v = \frac{2\pi d V_v}{\Gamma}$, $\epsilon = \frac{2\pi\varepsilon d^2}{\Gamma}$, $\omega = \frac{2\pi\varpi d^2}{\Gamma}$ where d, Γ, V_v, ε, ϖ denote, respectively, half the initial distance between the vortices, their strengths, the moving frame velocity, the strength of the strain field and its frequency. In particular ϵ here is ϵ/γ in Eq. (2.3) and (2.4) of Ref. 39 and ω here is $1/\gamma$ there.
[52] To speed up the numerical computations of the passive particles that are placed very close to the vortices we replace the small denominators in the velocity field by a cut off value of 0.01.
[53] Except the particles placed on the positive x axis.
[54] More generally, for a CS moving with some velocity $v_{cs}(t)$, as long as $\int_{t_1-t_0}^{t_1-t_0+\tau} v_{cs}(t)dt \cdot \mathbf{r}$ is growing sufficiently fast the same conclusions apply.
[55] To create the OVP figures we seed the square domain $[-2.5, 2.5] \times [-2.5, 2.5]$ by uniformly spaced 200^2 initial values, integrating the equations of motion with the Matlab ode45 solver.
[56] Y. Lehahn, F. d'Ovidio, M. Lévy, Y. Amitai, and E. Heifetz, "Long range transport of a quasi isolated chlorophyll patch by an Agulhas ring," Geophys. Res. Lett. **38**(16), L16610 (2011).
[57] F. J. Beron-Vera, Y. Wang, M. J. Olascoaga, G. J. Goni, and G. Haller, "Objective detection of oceanic eddies and the Agulhas leakage," J. Phys. Oceanogr. **43**, 1426–1438 (2013).
[58] G. Haller, "Lagrangian coherent structures from approximate velocity data," Phys. Fluids **14**, 1851–1861 (2002).
[59] G. Froyland, C. Horenkamp, V. Rossi, N. Santitissadeekorn, and A. S. Gupta, "Three-dimensional characterization and tracking of an Agulhas ring," Ocean Modell. **52**, 69–75 (2012).
[60] G. Froyland, "An analytic framework for identifying finite-time coherent sets in time-dependent dynamical systems," Phys. D **250**, 1–19 (2013).
[61] M. Farazmand and G. Haller, "A variational theory of hyperbolic Lagrangian coherent structures," Phys. D **241**, 439–441 (2012).